Article

Fullerenes against COVID-19: Repurposing C_{60} and C_{70} to Clog the Active Site of SARS-CoV-2 Protease

Tainah Dorina Marforio *📱, **Edoardo Jun Mattioli** 📱, **Francesco Zerbetto and Matteo Calvaresi** *📱

Dipartimento di Chimica "Giacomo Ciamician", Alma Mater Studiorum-Università di Bologna, Via Francesco Selmi 2, 40126 Bologna, Italy; edoardojun.mattioli2@unibo.it (E.J.M.); francesco.zerbetto@unibo.it (F.Z.)
* Correspondence: tainah.marforio2@unibo.it (T.D.M.); matteo.calvaresi3@unibo.it (M.C.)

Abstract: The persistency of COVID-19 in the world and the continuous rise of its variants demand new treatments to complement vaccines. Computational chemistry can assist in the identification of moieties able to lead to new drugs to fight the disease. Fullerenes and carbon nanomaterials can interact with proteins and are considered promising antiviral agents. Here, we propose the possibility to repurpose fullerenes to clog the active site of the SARS-CoV-2 protease, M^{pro}. Through the use of docking, molecular dynamics, and energy decomposition techniques, it is shown that C_{60} has a substantial binding energy to the main protease of the SARS-CoV-2 virus, M^{pro}, higher than masitinib, a known inhibitor of the protein. Furthermore, we suggest the use of C_{70} as an innovative scaffold for the inhibition of SARS-CoV-2 M^{pro}. At odds with masitinib, both C_{60} and C_{70} interact more strongly with SARS-CoV-2 M^{pro} when different protonation states of the catalytic dyad are considered. The binding of fullerenes to M^{pro} is due to shape complementarity, i.e., vdW interactions, and is aspecific. As such, it is not sensitive to mutations that can eliminate or invert the charges of the amino acids composing the binding pocket. Fullerenic cages should therefore be more effective against the SARS-CoV-2 virus than the available inhibitors such as masinitib, where the electrostatic term plays a crucial role in the binding.

Keywords: C_{60}; C_{70}; masitinib; M^{pro}; SARS-CoV-2; COVID-19; drug repurposing; MM-GBSA; inhibitors; nanobio interface

1. Introduction

The onslaught of COVID-19 waves and the continuous rise of variants of the SARS-CoV-2 virus [1] demand new treatments to complement vaccinations. Endocytic entry into host cells, RNA replication and transcription, translation and proteolytic processing of viral proteins, virion assembly, and release of new viruses through exocytic mechanisms are all potentially targetable processes in the coronavirus life cycle [2].

Among the viral proteins, only a few are essential in the life cycle of the virus. The main protease, known as M^{pro} or $3CL^{pro}$, plays a critical function in viral replication and transcription and represents the main target for medicinal chemistry [3,4]. This enzyme breaks down the polyprotein chain coded by the RNA of the virus into functional proteins, which the virus needs to construct itself and proliferate [3,4]. Disrupting this important part of the virus's self-replication engine blocks the infection.

Just a few weeks after the first COVID-19 outbreak, the crystallographic structure of M^{pro} was determined and deposited under the PDB code 6LU7 [3]. M^{pro} is composed of 306 amino acids, characterized by 3 distinct domains (domains I, II, and III) [3]. Domain I (residues 8–101) and domain II (residues 102–184) have a similar fold composed of antiparallel ß-barrel structures. Domain III (residues 201–303), instead, consists of a cluster of five α-helices, responsible for protein dimerization. The active site is placed in a cleft between domains I and II (Figure 1). The catalytic residues Cys145 and His41 are buried in this cavity that can accommodate four substrate residues in positions P1′ through

P4 and is flanked by residues from both domains I and II (Figure 1B). The catalytic dyad may be activated by a proton transfer from Cys145 to His41, possibly triggered by substrate binding or occurring in a transition state during the attack by the sulfur on the carbonyl carbon atom of the scissile peptide bond. It was suggested that a water molecule might complete the catalytic triad by mediating crucial interactions between His41 and other important conserved residues, such as His164 and Asp187 [4].
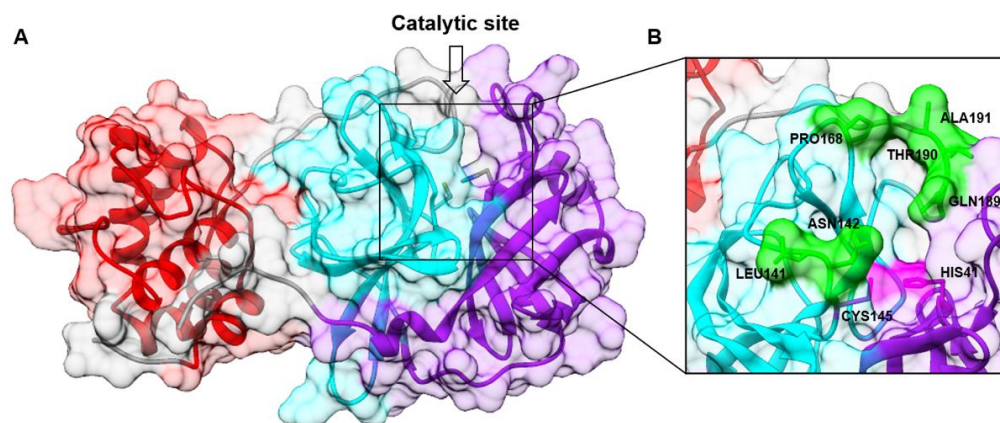
Figure 1. (**A**) M^{pro} structure (PDB ID 7JU7) shown in ribbons and surface representation: domain I (residues 8–101) in purple, domain II (residues 102–184) in cyan, and domain III (residues 201–303) in red. (**B**) A magnification of the catalytic site showing the catalytic dyad (His41 and Cys145) in purple and residues that lie within the binding pocket in green.

Due to the immediate availability of the M^{pro} crystal structure, structure-based drug discovery (SBDD) techniques were promptly used to expedite the rational identification of potential M^{pro} inhibitors [5–7] or to drive the repurposing of known molecules [8–14]. Many protease inhibitors of the human immunodeficiency virus (HIV) were identified as possible anti-COVID candidates [15].

Fullerenes and carbon nanomaterials are able to interact with peptides [16,17] and proteins [18–26] and, in general, are considered promising antiviral agents [27–32]. The idea of using C$_{60}$ as an inhibitor of the HIV protease dates back to 1993 [33]. C$_{60}$ inhibits the protein thanks to its size and unusual spherical shape [33]. The buckyball fits snugly into the substrate binding pocket, blocks the active site, and prevents the HIV polypeptide chain from entering [33]. C$_{60}$ is, however, insoluble in water, and fullerene derivatives were designed and then synthesized for use in a physiological environment [34–44]. The structure–activity relationship between functionalized fullerenes and HIV protease inhibition showed the importance of positioning the derivative moieties in a well-defined geometry on the fullerene cage [34–44].

The idea of repositioning C$_{60}$ for the inhibition of SARS-CoV-2 M^{pro} is a natural consequence [45–47]. In this work, we compare (i) the binding energy of C$_{60}$ with the HIV protease and with SARS-CoV-2 M^{pro} to understand the efficiency of the repurposing, and (ii) the performances of C$_{60}$ and masitinib [48], a known inhibitor of SARS-CoV-2 M^{pro}, to verify the possibility of using C$_{60}$ derivatives as effective M^{pro} inhibitors. We further propose, for the first time, the use of C$_{70}$ as an innovative scaffold for the inhibition of SARS-CoV-2 M^{pro}.

2. Results

2.1. Determining the C$_{60}$ Binding Pocket in SARS-CoV-2 M^{pro}

The crystal structures of SARS-CoV-2 M^{pro} complexed with different ligands (Figure 2A) showed that noncovalent and covalent inhibitors behave differently. Noncovalent inhibitors interact with the multiple residue system of the substrate binding pocket of SARS-CoV-2 M^{pro}. Covalent inhibitors mainly interact with the catalytic Cys145 residue after an initial noncovalent interaction in the substrate binding pocket.
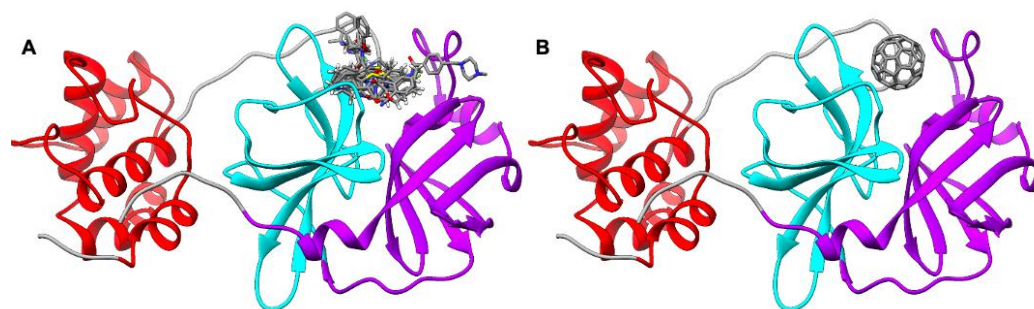
Figure 2. (**A**) Binding of M^{pro} ligands N3 (PDB ID 6LU7), masitinib (PDB ID 7JU7), parampanel analogue compound 5 (PDB ID 7L11), MPI4 (PDB ID 7JQ1), ML188 (PDB ID 7L0D), isofloxythepin (PDB ID 7AY7), carmofur (PDB ID 7BUY), UAW243 (PDB ID 6XFN), and boceprevir (PDB ID 6XQU) in M^{pro}. The protein structure is shown with the ribbon. (**B**) Identification of the fullerene binding pocket in M^{pro}.

Using a docking protocol able to identify the fullerene binding pockets of proteins [18,19,49–54], we docked the C$_{60}$ in SARS-CoV-2 M^{pro}. C$_{60}$ binds on the substrate binding pocket of M^{pro} (Figure 2B). The fullerene cage shows a strong shape complementarity with this pocket of M^{pro}. C$_{60}$ occupies exactly the same position occupied by known M^{pro} inhibitors, suggesting an inhibitory activity of the cage.

2.2. Determining the Binding Energy between C$_{60}$ and SARS-CoV-2 M^{pro}

The atomistic understanding of the interactions of C$_{60}$ with SARS-CoV-2 M^{pro} is crucial for real applications of nanomolecules in medicine [26]. MD simulations represent a powerful tool to investigate such interactions [55]. Starting from the docking pose, 100 ns of molecular dynamics simulations was carried out. To estimate the binding energy between M^{pro} and C$_{60}$, an MM-GBSA analysis of the trajectories was performed. C$_{60}$ lies above His41, giving sandwich-like π–π interactions [56,57], and interacts hydrophobically [56,57] with Met49 and Leu27. Surfactant-like interactions [56,57] with Cys145 and Ser46 are also observed.

The ΔG$_{binding}$ between M^{pro} and C$_{60}$ is −18.8 kcal mol^{-1}. This value is very close to the interaction energy between lysozyme and C$_{60}$ (−18.5 kcal mol^{-1}) [50], a complex that is experimentally accessible and widely used in nanomedicine [49,58–60]. The result demonstrates the feasibility of the exploitation of the C$_{60}$ molecule in the inhibition of M^{pro}.

According to the analysis of the binding components of the energy, the driving force for binding (−44.8 kcal mol^{-1}) is represented by van der Waals interactions. Hydrophobic interactions, (E$_{non-polar}$), assist the binding, despite the fact that their value (−2.5 kcal mol^{-1}) is far lower than that of the vdW interactions. The contributions of polar solvation (12.8 kcal mol^{-1}) and entropy (15.7 kcal mol^{-1}) are positive and oppose the binding. Because of the rigidity of CNPs, the entropic term is frequently overlooked [45] while studying protein–CNP interactions. However, this factor, which is estimated to be 15.7 kcal mol^{-1}, is energetically significant and should be considered when protein–CNP hybrids are studied. The binding of C$_{60}$ to the protein cavity produces a significant reduction in amino acid mobility, giving rise to this high value.

The decomposition analysis of the total binding energy provides the contribution to the binding of each amino acid (Figure 3). The most interacting amino acids (ΔG$_{binding}$ larger than 1.0 kcal mol^{-1}) are Met49, His41, Ser46, Leu27, and Cys145. Very interestingly, C$_{60}$ strongly interacts both with the catalytic dyad (Cys145-His 41) and with residues located on the substrate binding pocket (Met49, Ser46, Leu27).
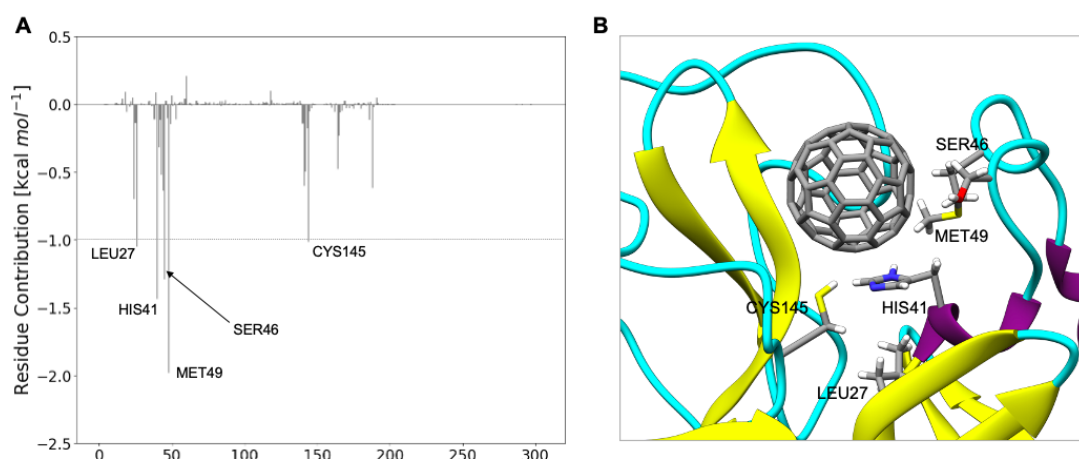
Figure 3. (**A**) C_{60}@M^{pro} interactions. $\Delta G_{binding}$ decomposed *per* residue. (**B**) Interaction between Met49, His41, Ser46, Leu27, and Cys145 and C_{60}.

At the same time, C_{60} shields the catalytic dyad, blocking its catalytic activity, and occupies the substrate binding pocket, impeding the interaction of M^{pro} with its substrate.

2.3. Comparing the Binding of C_{60} in SARS-CoV-2 M^{pro} and HIV Protease

To validate the results and evaluate the reliability of the use of C_{60} as an M^{pro} inhibitor, we calculated the interaction of C_{60} with the HIV protease (Pro$_{HIV}$), using the same protocol adopted to calculate the binding energy between C_{60} and M^{pro} (Table 1).

Table 1. Energy components of $\Delta G_{binding}$ (VDW, E_{el}, E_{GB}, and $E_{non\text{-}polar}$) for C_{60}@M^{pro} and C_{60}@Pro$_{HIV}$ complexes. All energies are reported in kcal mol^{-1}.

Complex	ΔH	VDW	E_{El}	E_{GB}	$E_{non\text{-}polar}$	TΔS	ΔG_{bind}
C_{60}@M^{pro}	−34.5	−44.8	0.0	12.8	−2.5	−15.7	−18.8
C_{60}@Pro$_{HIV}$	−38.0	−51.6	0.0	16.0	−2.4	−18.3	−19.7

Shape complementarity is the crucial parameter governing the interaction of fullerene with proteins [57]. In Pro$_{HIV}$, as well as in M^{pro}, C_{60} fits snugly in the active site (Figure 4), and as a consequence, the total binding energy and the energy components of $\Delta G_{binding}$ between C_{60} and the two proteases are similar [61].
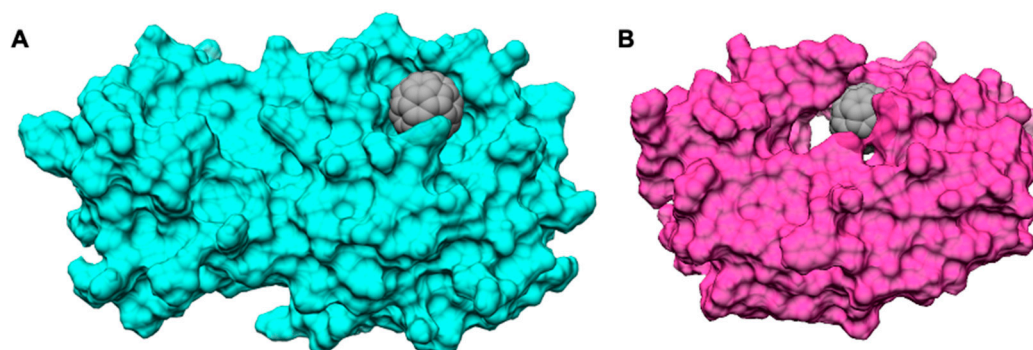

Figure 4. Surface complementarity between (**A**) M^{pro} and (**B**) Pro$_{HIV}$ proteins and the C_{60} cage.

Since it is known that C_{60} experimentally works as an HIV protease inhibitor [33–44], this comparison validates the idea of repurposing C_{60} as a SARS-CoV-2 M^{pro} inhibitor.

2.4. Comparing the Binding of C_{60} in SARS-CoV-2 M^{pro} with Masitinib

To estimate the potential application of C_{60} as an inhibitor of M^{pro}, we calculated the binding energy with a known inhibitor of M^{pro}, namely, masitinib. Masitinib is an orally bioavailable tyrosine kinase inhibitor, repurposed as an inhibitor of SARS-CoV-2 M^{pro} [48]. X-ray crystallography and biochemistry experiments showed that masitinib acts as a competitive inhibitor of M^{pro} [48] and occupies the same binding pocket of C_{60} (Figure 5). Mice infected with SARS-CoV-2 and subsequently treated with masitinib had a 200-fold decrease in viral titers in the lungs and nose, as well as lower lung inflammation [48].
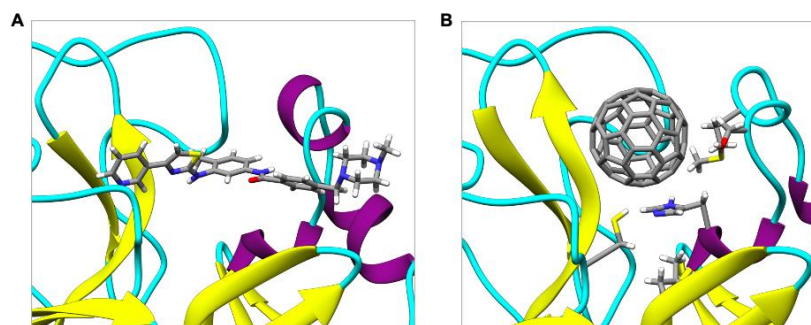
Figure 5. Binding of (**A**) masitinib and (**B**) C_{60} with M^{pro}.

The results show that C_{60} has a larger binding energy than masitinib, due to two factors that are usually ignored when the interactions between inhibitors and proteins are evaluated, namely, desolvation energy and entropy (Table 2).
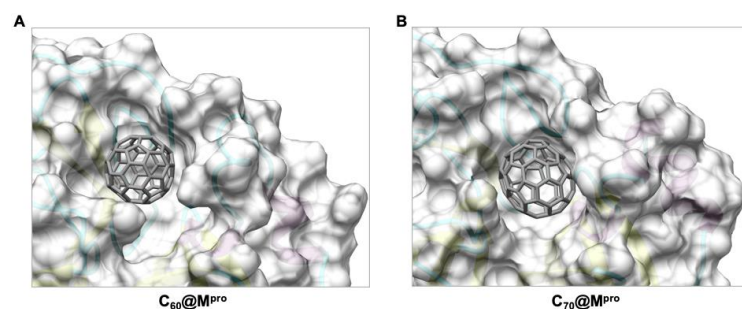
Table 2. Energy components of $\Delta G_{binding}$ (VDW, E_{el}, E_{GB}, and $E_{non-polar}$) for $C_{60}@M^{pro}$ and masitinib$@M^{pro}$ complexes. All energies are reported in kcal mol^{-1}.

Complex	ΔH	VDW	E_{El}	E_{GB}	$E_{non-polar}$	$T\Delta S$	ΔG_{bind}
$C_{60}@M^{pro}$	−34.5	−44.8	0.0	12.8	−2.5	−15.7	−18.8
masitinib$@M^{pro}$	−41.2	−51.4	−18.1	34.0	−5.8	−24.7	−16.5

Even if vdW and electrostatic terms are larger for masitinib than for C_{60}, binding of the more polar and more flexible masitinib molecule gives larger penalty terms due to the desolvation energy and entropy. C_{60} is an ideal inhibitor because the terms that generally oppose binding (i.e., desolvation energy and entropy) are minimized by its hydrophobicity and rigidity.

2.5. Determining the Binding Energy between C_{70} and SARS-CoV-2 M^{pro}

With the increase in the carbon cage size, the binding strength between proteins and fullerenes usually increases [60,62]. It is natural to suppose that C_{70}, in principle, may be a better inhibitor than C_{60} for M^{pro}. Docking calculations showed that C_{70} occupies the same binding pocket (Figure 6).


Figure 6. Surface representation of the binding cleft of (**A**) C_{60} and (**B**) C_{70} in M^{pro}.

The $\Delta G_{binding}$ between C_{70} and M^{pro} is considerably higher (-28.0 kcal mol^{-1}) than in the case of C_{60} (-18.8 kcal mol^{-1}) (Table 3).

Table 3. Energy components of $\Delta G_{binding}$ (VDW, E_{el}, E_{GB}, and $E_{non-polar}$) for $C_{60}@M^{pro}$ and $C_{70}@M^{pro}$ complexes. All energies are reported in kcal mol^{-1}.

Complex	ΔH	VDW	E_{El}	E_{GB}	$E_{non-polar}$	$T\Delta S$	ΔG_{bind}
$C_{60}@M^{pro}$	-34.5	-44.8	0.0	12.8	-2.5	-15.7	-18.8
$C_{70}@M^{pro}$	-45.6	-59.2	0.0	16.8	-3.2	-17.6	-28.0

This increase is due to a substantial increase in the van der Waals interactions, which grow from -44.8 kcal mol^{-1} for C_{60} to -59.2 kcal mol^{-1} for C_{70}. Van der Waals and hydrophobic interactions are -47.3 kcal mol^{-1} in C_{60} and -62.4 kcal mol^{-1} in C_{70}, with a net increase of 15.1 kcal mol^{-1}. In C_{70}, the increase compensates the small energy penalties due to higher entropic and desolvation terms (28.5 kcal mol^{-1} in C_{60} and 34.4 kcal mol^{-1} in C_{70}, with a net increase of 5.9 kcal mol^{-1}). The measure of shape complementarity between the fullerene cage and the protein is usually taken as a quick way to estimate the stabilizing interactions. This is also true in this case considering that the variation in the solvent-accessible surface area (ΔSASA) upon binding is 347.2 Å^2 for $C_{60}@M^{pro}$ and 444.4 Å^2 for $C_{70}@M^{pro}$, as evident also in Figure 6. The larger C_{70} engages stronger interactions with a larger number of the amino acids that make up the binding pocket (Figure 7). The interactions of C_{60} with the catalytic dyad of His41 and Cys145 are -1.4 kcal mol^{-1} and -1.0 kcal mol^{-1}, respectively. The interactions of C_{70} with the same residues are -2.3 kcal mol^{-1} and -1.3 kcal mol^{-1}, with an increase of 0.9 kcal mol^{-1} and 0.3 kcal mol^{-1}. In addition, C_{70} also strongly interacts with Met165 (-1.5 kcal mol^{-1}) and Gln189 (-1.5 kcal mol^{-1}), residues that were identified as the hot spot for the activity of M^{pro} inhibitors [63].
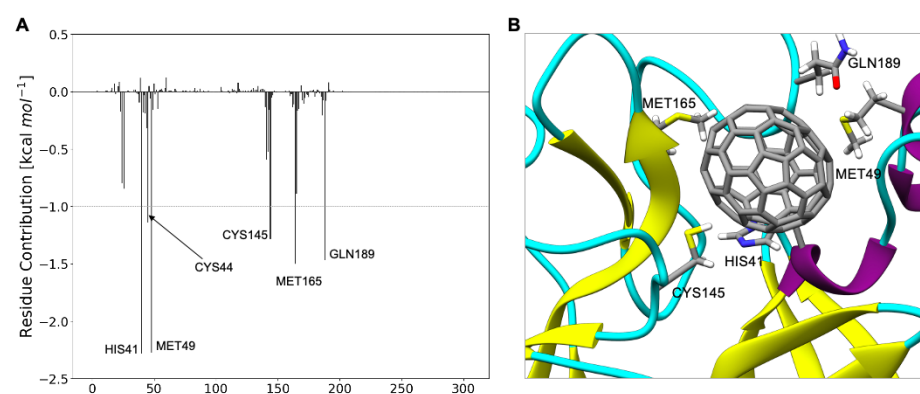
Figure 7. (A) $C_{70}@M^{pro}$ interactions. $\Delta G_{binding}$ decomposed *per* residue. (B) Interaction between His41, Cys44, Met49, Cys145, Met165, and Gln189 and C_{70}.

2.6. Evaluating the Binding Enrgy of Masitinib, C_{60}, and C_{70} to SARS-CoV-2 M^{pro} in Different Protonation States of the Catalytic Dyad

The protonation state of histidine [64–67], and in particular of the catalytic dyad (His41-Cys145), plays a crucial role in M^{pro} activity, stability, and protein–ligand interactions. Very recently, neutron crystallographic studies [65,67] provided direct visualization of the hydrogen atoms' locations in the SARS-CoV-2 M^{pro} enzyme. If in the bound state His41 is in a neutral form [65], in the ligand-free structure, the catalytic site of M^{pro} adopts a zwitterionic form where Cys145 is deprotonated and negatively charged and His41 is doubly protonated and positively charged [67]. Since the free energy of activation for the initial proton transfer from Cys145 to His41 is very low [68,69] and the relative energies of the zwitterionic and neutral states are very close [68,69], we reinvestigated the binding of masitinib, C_{60}, and C_{70} to M^{pro} in both protonation states of the catalytic dyad (Table 4).

Table 4. Comparison of the binding energy of masitinib, C_{60}, and C_{70} with M^{pro} in the two protomeric states, namely, His41-Cys145 and His41$^+$-Cys145$^-$. All energies are reported in kcal mol^{-1}.

Complex	His41-Cys145 $\Delta G_{binding}$	His41$^+$-Cys145-$\Delta G_{binding}$
masitinib@M^{pro}	−16.5	−5.1
C_{60}@M^{pro}	−18.8	−24.3
C_{70}@M^{pro}	−28.0	−29.4

The protonation state of the catalytic dyad strongly affects the binding of masitinib, and in the zwitterionic form (His41$^+$-Cys145$^-$), the $\Delta G_{binding}$ is markedly reduced (going from −15.5 kcal mol^{-1} to −5.1 kcal mol^{-1}). The electrostatic term decreases from −18.1 kcal mol^{-1} for the doubly neutral dyad to −11.0 kcal mol^{-1} for the zwitterionic dyad, due to the different distributions of the charges in the binding site. This term is unaffected in the fullerene binding because it does not have net charges. Owing to increased vdW interactions, $\Delta G_{binding}$ of fullerenes increases in the case of the zwitterionic form of the dyad. It goes from −44.8 kcal mol^{-1} to −54.6 kcal mol^{-1} for C_{60} and from −59.2 kcal mol^{-1} to −60.9 kcal mol^{-1} for C_{70}.

3. Conclusions

In summary, we demonstrated the possibility of repurposing fullerenes as inhibitors of SARS-CoV-2 M^{pro}. We calculated and compared the binding energies of (a) C_{60} and C_{70} to M^{pro}, (b) C_{60} to the HIV protease, and (c) masitinib to M^{pro}. The results indicate the feasibility of the repurposing. Fingerprint analysis showed the role of π–π, hydrophobic, and surfactant-like interactions in the binding of the fullerenes to M^{pro}. Fullerenes interact with the His41-Cys145 dyad, blocking the catalytic activity. At the same time, they occupy the substrate binding pocket, impeding the interaction of M^{pro} with its substrate.

Fullerenes are ideal inhibitors because, in these molecules, the terms that generally oppose the binding (i.e., desolvation energy and entropy) are minimized by their hydrophobicity and rigidity.

Shape complementarity is crucial to govern the interaction of fullerenes with proteins, and also in this case, the larger C_{70} interacts more strongly than C_{60} with the binding site of M^{pro}. C_{70} engages stronger interactions with more residues that form the binding pocket. In particular, C_{70} strongly interacts with the Met165 and Gln189 residues that were identified as the hot spot for the activity of M^{pro} inhibitors.

Fullerenes are insensitive to mutations that perturb the electrostatic characteristics of the binding site. They interact even more strongly with M^{pro} when different protonation states of the catalytic dyad are considered.

The binding of fullerenes to M^{pro}, based as it is on shape complementarity, i.e., vdW interactions, is aspecific. As such, it is not sensitive to mutations that eliminate or invert the charges of the amino acids composing the binding pocket. Indeed, for some inhibitors, such as masinitib, the electrostatic terms play a crucial role. As a consequence, even a punctual modification of the catalyic site may strongly affect their binding, and therefore their activity. Fullerenes therefore appear to be ideal moieties to exploit in the identification of potential new drugs against the SARS-CoV-2 protease and other viral proteins.

4. Materials and Methods

4.1. System Setup

The crystal structures of the SARS-CoV-2 main proteases (PDB ID 6LU7, 7JU7, and 7L10) and the HIV protease (PDB ID 1ZTZ) were downloaded from the Protein Data Bank (PDB). The crystal structure of PDB ID 7JU7 was used for the docking calculations.

The Amber ff14SB force field [70] was used to model the M^{pro} and Pro_{HIV} proteins. C_{60} and C_{70} carbon atoms were modeled as uncharged Lennard-Jones particles by using sp2 carbon parameters taken from the ff14SB force field [70]. Masitinib was parametrized by calculating the partial atomic charges using the restraint electrostatic potential method (RESP)

at the HF/6-31G* level of theory. The corresponding parameters were then generated by the standard procedure reported for antechamber, as implemented in Amber16 [71].

4.2. Docking

Docking models were obtained using the PatchDock algorithm [72] that computes the shape complementarity between two entities (ligand and receptor), minimizing the number of steric clashes. PatchDock (i) assigns concave, convex, or flat patches to the ligand and receptor surface, (ii) matches concave–convex/flat–flat, and generates a set of candidate transformations. (iii) Each transformation is then ranked by the shape complementarity and the atomic desolvation energy of the complex (scoring functions). Root mean square deviation clustering avoids the generation of redundant solutions.

4.3. MD Simulations

The docking structures were minimized by 5000 steps of steepest descent minimization, followed by 5000 steps of the conjugate gradient algorithm. The minimized structures underwent a 1 ns equilibration step and were heated from 0 to 300 K (Langevin thermostat). Periodic boundary conditions (PBC) and particle mesh Ewald summation were used throughout (with a cut-off radius of 10 Å for the direct space sum). The MD simulations were carried out using an explicit solvent (TIP3P water model). Sodium counterions were included to exactly neutralize the charge of the system. After the equilibration, a production MD simulation of 100 ns was carried out for every system at 300 K. Amber 16 was used to run all the simulations [71].

4.4. Molecular Mechanics/Generalized Born Surface Area (MM/GBSA) Analysis

A total of 5000 frames were extracted from MD simulations and used for the MM-GBSA analysis. An infinite cut-off was used for all the interactions. The electrostatic contribution to the solvation free energy was calculated with the Generalized Born (GB) model, as implemented in MMPBSA.py [73]. The nonpolar contribution to the solvation free energy was determined with solvent-accessible surface-area-dependent terms. To obtain an estimate of the binding entropy, the normal modes for the complex, receptor, and ligand were calculated, and the results were averaged using the PTRAJ program (Normal Mode Analysis) via MMPBSA.py [73].

Author Contributions: Conceptualization, M.C.; methodology, M.C and T.D.M.; investigation, T.D.M. and E.J.M.; data curation, T.D.M.; supervision, M.C.; writing—original draft, T.D.M. and M.C.; writing—review and editing, T.D.M., E.J.M., F.Z. and M.C. All authors have read and agreed to the published version of the manuscript.

Data Availability Statement: All data in this study can be requested from the corresponding authors (tainah.marforio2@unibo.it, T.D.M.; matteo.calvaresi3@unibo.it, M.C.).

Conflicts of Interest: The authors declare no conflict of interest.

References

1. Li, J.; Lai, S.; Gao, G.F.; Shi, W. The emergence, genomic diversity and global spread of SARS-CoV-2. *Nature* **2021**, *600*, 408–418. [CrossRef]
2. V'kovski, P.; Kratzel, A.; Steiner, S.; Stalder, H.; Thiel, V. Coronavirus biology and replication: Implications for SARS-CoV-2. *Nat. Rev. Microbiol.* **2021**, *19*, 155–170. [CrossRef]
3. Jin, Z.; Du, X.; Xu, Y.; Deng, Y.; Liu, M.; Zhao, Y.; Zhang, B.; Li, X.; Zhang, L.; Peng, C.; et al. Structure of Mpro from SARS-CoV-2 and discovery of its inhibitors. *Nature* **2020**, *582*, 289–293. [CrossRef]
4. Kneller, D.W.; Phillips, G.; O'Neill, H.M.; Jedrzejczak, R.; Stols, L.; Langan, P.; Joachimiak, A.; Coates, L.; Kovalevsky, A. Structural plasticity of SARS-CoV-2 3CL Mpro active site cavity revealed by room temperature X-ray crystallography. *Nat. Commun.* **2020**, *11*, 7–12. [CrossRef]
5. Zhang, L.; Lin, D.; Sun, X.; Curth, U.; Drosten, C.; Sauerhering, L.; Becker, S.; Rox, K.; Hilgenfeld, R. Crystal structure of SARS-CoV-2 main protease provides a basis for design of improved a-ketoamide inhibitors. *Science* **2020**, *368*, 409–412. [CrossRef]

6. Dai, W.; Zhang, B.; Jiang, X.M.; Su, H.; Li, J.; Zhao, Y.; Xie, X.; Jin, Z.; Peng, J.; Liu, F.; et al. Structure-based design of antiviral drug candidates targeting the SARS-CoV-2 main protease. *Science* **2020**, *368*, 1331–1335. [CrossRef]

7. Wang, Z.; Yang, L.; Zhao, X.E. Co-crystallization and structure determination: An effective direction for anti-SARS-CoV-2 drug discovery. *Comput. Struct. Biotechnol. J.* **2021**, *19*, 4684–4701. [CrossRef]

8. Harrison, C. Coronavirus puts drug repurposing on the fast track. *Nat. Biotechnol.* **2020**, *38*, 379–381. [CrossRef]

9. Sarkar, A.; Mandal, K. Repurposing an Antiviral Drug against SARS-CoV-2 Main Protease. *Angew. Chem. Int. Ed.* **2021**, *60*, 23492–23494. [CrossRef]

10. Gupta, A.; Zhou, H.X. Profiling SARS-CoV-2 Main Protease (MPRO) Binding to Repurposed Drugs Using Molecular Dynamics Simulations in Classical and Neural Network-Trained Force Fields. *ACS Comb. Sci.* **2020**, *22*, 826–832. [CrossRef]

11. Kuzikov, M.; Costanzi, E.; Reinshagen, J.; Esposito, F.; Vangeel, L.; Wolf, M.; Ellinger, B.; Claussen, C.; Geisslinger, G.; Corona, A.; et al. Identification of Inhibitors of SARS-CoV-2 3CL-Pro Enzymatic Activity Using a Small Molecule in Vitro Repurposing Screen. *ACS Pharmacol. Transl. Sci.* **2021**, *4*, 1096–1110. [CrossRef]

12. Hasan, M.; Parvez, M.S.A.; Azim, K.F.; Imran, M.A.S.; Raihan, T.; Gulshan, A.; Muhit, S.; Akhand, R.N.; Ahmed, S.S.U.; Uddin, M.B. Main protease inhibitors and drug surface hotspots for the treatment of COVID-19: A drug repurposing and molecular docking approach. *Biomed. Pharmacother.* **2021**, *140*, 111742. [CrossRef]

13. Pinzi, L.; Tinivella, A.; Caporuscio, F.; Rastelli, G. Drug Repurposing and Polypharmacology to Fight SARS-CoV-2 Through Inhibition of the Main Protease. *Front. Pharmacol.* **2021**, *12*, 636989. [CrossRef]

14. Macip, G.; Garcia-Segura, P.; Mestres-Truyol, J.; Saldivar-Espinoza, B.; Ojeda-Montes, M.J.; Gimeno, A.; Cereto-Massagué, A.; Garcia-Vallvé, S.; Pujadas, G. Haste makes waste: A critical review of docking-based virtual screening in drug repurposing for SARS-CoV-2 main protease (M-pro) inhibition. *Med. Res. Rev.* **2022**, *42*, 744–769. [CrossRef]

15. Zhu, W.; Shyr, Z.; Lo, D.C.; Zheng, W. Viral proteases as targets for coronavirus disease 2019 drug development. *J. Pharmacol. Exp. Ther.* **2021**, *378*, 166–172. [CrossRef]

16. Di Giosia, M.; Nicolini, F.; Ferrazzano, L.; Soldà, A.; Valle, F.; Cantelli, A.; Marforio, T.D.; Bottoni, A.; Zerbetto, F.; Montalti, M.; et al. Stable and Biocompatible Monodispersion of C 60 in Water by Peptides. *Bioconjug. Chem.* **2019**, *30*, 808–814. [CrossRef]

17. Rozhin, P.; Charitidis, C.; Marchesan, S. Self-assembling peptides and carbon nanomaterials join forces for innovative biomedical applications. *Molecules* **2021**, *26*, 4084. [CrossRef]

18. Calvaresi, M.; Zerbetto, F. Baiting proteins with C60. *ACS Nano* **2010**, *4*, 2283–2299. [CrossRef]

19. Calvaresi, M.; Zerbetto, F. Fullerene sorting proteins. *Nanoscale* **2011**, *3*, 2873–2881. [CrossRef]

20. De Leo, F.; Magistrato, A.; Bonifazi, D. Interfacing proteins with graphitic nanomaterials: From spontaneous attraction to tailored assemblies. *Chem. Soc. Rev.* **2015**, *44*, 6916–6953. [CrossRef]

21. Calvaresi, M.; Zerbetto, F. The Devil and Holy Water: Protein and Carbon Nanotube Hybrids. *Acc. Chem. Res.* **2013**, *46*, 2454–2463. [CrossRef]

22. Marchesan, S.; Prato, M. Under the lens: Carbon nanotube and protein interaction at the nanoscale. *Chem. Commun.* **2015**, *51*, 4347–4359. [CrossRef]

23. Di Giosia, M.; Valle, F.; Cantelli, A.; Bottoni, A.; Zerbetto, F.; Fasoli, E.; Calvaresi, M. High-throughput virtual screening to rationally design protein—Carbon nanotube interactions. Identification and preparation of stable water dispersions of protein—Carbon nanotube hybrids and efficient design of new functional materials. *Carbon N. Y.* **2019**, *147*, 70–82. [CrossRef]

24. Di Giosia, M.; Marforio, T.D.; Cantelli, A.; Valle, F.; Zerbetto, F.; Su, Q.; Wang, H.; Calvaresi, M. Inhibition of α-chymotrypsin by pristine single-wall carbon nanotubes: Clogging up the active site. *J. Colloid Interface Sci.* **2020**, *571*, 174–184. [CrossRef]

25. Rozhin, P.; Abdel Monem Gamal, J.; Giordani, S.; Marchesan, S. Carbon Nanomaterials (CNMs) and Enzymes: From Nanozymes to CNM-Enzyme Conjugates and Biodegradation. *Materials* **2022**, *15*, 1037. [CrossRef]

26. Di Costanzo, L.; Geremia, S. Atomic details of carbon-based nanomolecules interacting with proteins. *Molecules* **2020**, *25*, 3555. [CrossRef]

27. Reina, G.; Peng, S.; Jacquemin, L.; Andrade, A.F.; Bianco, A. Hard Nanomaterials in Time of Viral Pandemics. *ACS Nano* **2020**, *14*, 9364–9388. [CrossRef]

28. Serrano-Aroca, Á.; Takayama, K.; Tuñón-Molina, A.; Seyran, M.; Hassan, S.S.; Pal Choudhury, P.; Uversky, V.N.; Lundstrom, K.; Adadi, P.; Palù, G.; et al. Carbon-Based Nanomaterials: Promising Antiviral Agents to Combat COVID-19 in the Microbial-Resistant Era. *ACS Nano* **2021**, *15*, 8069–8086. [CrossRef]

29. Mallakpour, S.; Azadi, E.; Hussain, C.M. Fight against COVID-19 pandemic with the help of carbon-based nanomaterials. *New J. Chem.* **2021**, *45*, 8832–8846. [CrossRef]

30. Innocenzi, P.; Stagi, L. Carbon-based antiviral nanomaterials: Graphene, C-dots, and fullerenes. A perspective. *Chem. Sci.* **2020**, *11*, 6606–6622. [CrossRef]

31. Sengupta, J.; Hussain, C.M. Carbon nanomaterials to combat virus: A perspective in view of COVID-19. *Carbon Trends* **2021**, *2*, 100019. [CrossRef]

32. Khan, A.; Ahsan, O.; Wei, D.Q.; Ansari, J.K.; Najmi, M.H.; Muhammad, K.; Waheed, Y. Computational evaluation of abrogation of hbx-bcl-xl complex with high-affinity carbon nanotubes (Fullerene) to halt the hepatitis b virus replication. *Molecules* **2021**, *26*, 6433. [CrossRef]

33. Friedman, S.H.; DeCamp, D.L.; Kenyon, G.L.; Sijbesma, R.P.; Srdanov, G.; Wudl, F. Inhibition of the HIV-1 Protease by Fullerene Derivatives: Model Building Studies and Experimental Verification. *J. Am. Chem. Soc.* **1993**, *115*, 6506–6509. [CrossRef]

34. Sijbesma, R.; Srdanov, G.; Wudl, F.; Castoro, J.A.; Wilkins, C.; Friedman, S.H.; Decamp, D.L.; Kenyon, G.L. Synthesis of a Fullerene Derivative for the Inhibition of HIV Enzymes. *J. Am. Chem. Soc.* **1993**, 6510–6512. [CrossRef]

35. Schinazi, R.F.; Sijbesma, R.; Srdanov, G.; Hill, C.L.; Wudl, F. Synthesis and virucidal activity of a water-soluble, configurationally stable, derivatized C60 fullerene. *Antimicrob. Agents Chemother.* **1993**, *37*, 1707–1710. [CrossRef]

36. Nakamura, E.; Tokuyama, H.; Yamago, S.; Shiraki, T.; Sugiura, Y. Biological activity of water-soluble fullerenes. Structural dependence of DNA cleavage, cytotoxicity, and enzyme inhibitory activities including HIV-protease inhibition. *Bull. Chem. Soc. Jpn.* **1996**, *69*, 2143–2151. [CrossRef]

37. Friedman, S.H.; Ganapathi, P.S.; Rubin, Y.; Kenyon, G.L. Optimizing the Binding of Fullerene Inhibitors of the HIV-1 Protease through Predicted Increases in Hydrophobic Desolvation. *J. Med. Chem.* **1998**, *41*, 2424–2429. [CrossRef]

38. Luca Marcorin, G.; Da Ros, T.; Castellano, S.; Stefancich, G.; Bonin, I.; Miertus, S.; Prato, M. Design and synthesis of novel [60] fullerene derivatives as potential HIV aspartic protease inhibitors. *Org. Lett.* **2000**, *2*, 3955–3957. [CrossRef]

39. Bosi, S.; Da Ros, T.; Spalluto, G.; Balzarini, J.; Prato, M. Synthesis and anti-HIV properties of new water-soluble bis- functional-ized[60]fullerene derivatives. *Bioorg. Med. Chem. Lett.* **2003**, *13*, 4437–4440. [CrossRef]

40. Marchesan, S.; Da Ros, T.; Spalluto, G.; Balzarini, J.; Prato, M. Anti-HIV properties of cationic fullerene derivatives. *Bioorg. Med. Chem. Lett.* **2005**, *15*, 3615–3618. [CrossRef]

41. Troshina, O.A.; Troshin, P.A.; Peregudov, A.S.; Kozlovskiy, V.I.; Balzarini, J.; Lyubovskaya, R.N. Chlorofullerene C60Cl6: A precursor for straightforward preparation of highly water-soluble polycarboxylic fullerene derivatives active against HIV. *Org. Biomol. Chem.* **2007**, *5*, 2783–2791. [CrossRef]

42. Strom, T.A.; Durdagi, S.; Ersoz, S.S.; Salmas, R.E.; Supuran, C.T.; Barron, A.R. Fullerene-based inhibitors of HIV-1 protease. *J. Pept. Sci.* **2015**, *21*, 862–870. [CrossRef]

43. Yasuno, T.; Ohe, T.; Kataoka, H.; Hashimoto, K.; Ishikawa, Y.; Furukawa, K.; Tateishi, Y.; Kobayashi, T.; Takahashi, K.; Nakamura, S.; et al. Fullerene derivatives as dual inhibitors of HIV-1 reverse transcriptase and protease. *Bioorg. Med. Chem. Lett.* **2021**, *31*, 127675. [CrossRef]

44. Kobayashi, T.; Yasuno, T.; Takahashi, K.; Nakamura, S.; Mashino, T.; Ohe, T. Novel pyridinium-type fullerene derivatives as multitargeting inhibitors of HIV-1 reverse transcriptase, HIV-1 protease, and HCV NS5B polymerase. *Bioorg. Med. Chem. Lett.* **2021**, *49*, 128267. [CrossRef]

45. Hurmach, V.V.; Platonov, M.O.; Prylutska, S.V.; Scharff, P.; Prylutskyy, Y.I.; Ritter, U. C60 fullerene against SARS-CoV-2 coronavirus: An in silico insight. *Sci. Rep.* **2021**, *11*, 17748. [CrossRef]

46. Suárez, M.; Makowski, K.; Lemos, R.; Almagro, L.; Rodríguez, H.; Herranz, M.Á.; Molero, D.; Ortiz, O.; Maroto, E.; Albericio, F.; et al. An Androsterone-H2@C60 hybrid: Synthesis, Properties and Molecular Docking Simulations with SARS-Cov-2. *Chempluschem* **2021**, *86*, 972–981. [CrossRef]

47. Skariyachan, S.; Gopal, D.; Deshpande, D.; Joshi, A.; Uttarkar, A.; Niranjan, V. Carbon fullerene and nanotube are probable binders to multiple targets of SARS-CoV-2: Insights from computational modeling and molecular dynamic simulation studies. *Infect. Genet. Evol.* **2021**, *96*, 105155. [CrossRef]

48. Drayman, N.; DeMarco, J.K.; Jones, K.A.; Azizi, S.A.; Froggatt, H.M.; Tan, K.; Maltseva, N.I.; Chen, S.; Nicolaescu, V.; Dvorkin, S.; et al. Masitinib is a broad coronavirus 3CL inhibitor that blocks replication of SARS-CoV-2. *Science* **2021**, *373*, 931–936. [CrossRef]

49. Calvaresi, M.; Arnesano, F.; Bonacchi, S.; Bottoni, A.; Calò, V.; Conte, S.; Falini, G.; Fermani, S.; Losacco, M.; Montalti, M.; et al. C60@Lysozyme: Direct observation by nuclear magnetic resonance of a 1:1 fullerene protein adduct. *ACS Nano* **2014**, *8*, 1871–1877. [CrossRef]

50. Calvaresi, M.; Bottoni, A.; Zerbetto, F. Thermodynamics of Binding between Proteins and Carbon Nanoparticles: The Case of C60@Lysozyme. *J. Phys. Chem. C* **2015**, *119*, 28077–28082. [CrossRef]

51. Calvaresi, M.; Furini, S.; Domene, C.; Bottoni, A.; Zerbetto, F. Blocking the passage: C60 geometrically clogs K$^+$ channels. *ACS Nano* **2015**, *9*, 4827–4834. [CrossRef]

52. Trozzi, F.; Marforio, T.D.; Bottoni, A.; Zerbetto, F.; Calvaresi, M. Engineering the Fullerene-protein Interface by Computational Design: The Sum is More than its Parts. *Isr. J. Chem.* **2017**, *57*, 547–552. [CrossRef]

53. di Giosia, M.; Valle, F.; Cantelli, A.; Bottoni, A.; Zerbetto, F.; Calvaresi, M. C60 bioconjugation with proteins: Towards a palette of carriers for all pH ranges. *Materials* **2018**, *11*, 691. [CrossRef]

54. Bologna, F.; Mattioli, E.J.; Bottoni, A.; Zerbetto, F.; Calvaresi, M. Interactions between Endohedral Metallofullerenes and Proteins: The Gd@C$_{60}$–Lysozyme Model. *ACS Omega* **2018**, *3*, 13782–13789. [CrossRef]

55. Ganazzoli, F.; Raffaini, G. Classical atomistic simulations of protein adsorption on carbon nanomaterials. *Curr. Opin. Colloid Interface Sci.* **2019**, *41*, 11–26. [CrossRef]

56. Marforio, T.D.; Calza, A.; Mattioli, E.J.; Zerbetto, F.; Calvaresi, M. Dissecting the supramolecular dispersion of fullerenes by proteins/peptides: Amino acid ranking and driving forces for binding to c60. *Int. J. Mol. Sci.* **2021**, *22*, 11567. [CrossRef]

57. Di Giosia, M.; Zerbetto, F.; Calvaresi, M. Incorporation of Molecular Nanoparticles Inside Proteins: The Trojan Horse Approach in Theranostics. *Acc. Mater. Res.* **2021**, *8*, 594–605. [CrossRef]

58. Di Giosia, M.; Bomans, P.H.H.; Bottoni, A.; Cantelli, A.; Falini, G.; Franchi, P.; Guarracino, G.; Friedrich, H.; Lucarini, M.; Paolucci, F.; et al. Proteins as supramolecular hosts for C60: A true solution of C60 in water. *Nanoscale* **2018**, *10*, 9908–9916. [CrossRef]

59. Soldà, A.; Cantelli, A.; Di Giosia, M.; Montalti, M.; Zerbetto, F.; Rapino, S.; Calvaresi, M. C60@lysozyme: A new photosensitizing agent for photodynamic therapy. *J. Mater. Chem. B* **2017**, *5*, 6608–6615. [CrossRef]

60. Di Giosia, M.; Soldà, A.; Seeger, M.; Cantelli, A.; Arnesano, F.; Nardella, M.I.; Mangini, V.; Valle, F.; Montalti, M.; Zerbetto, F.; et al. A Bio-Conjugated Fullerene as a Subcellular-Targeted and Multifaceted Phototheranostic Agent. *Adv. Funct. Mater.* **2021**, *31*, 2101527. [CrossRef]

61. Martínez-Ortega, U.; Figueroa-Figueroa, D.I.; Hernández-Luis, F.; Aguayo-Ortiz, R. In Silico Characterization of Masitinib Interaction with SARS-CoV-2 Main Protease. *ChemMedChem* **2021**, *16*, 2339–2344. [CrossRef]

62. Wu, X.; Yang, S.T.; Wang, H.; Wang, L.; Hu, W.; Cao, A.; Liu, Y. Influences of the size and hydroxyl number of fullerenes/fullerenols on their interactions with proteins. *J. Nanosci. Nanotechnol.* **2010**, *10*, 6298–6304. [CrossRef]

63. Luo, S.; Huang, K.; Zhao, X.; Cong, Y.; Zhang, J.Z.H.; Duan, L. Inhibition mechanism and hot-spot prediction of nine potential drugs for SARS-CoV-2 Mproby large-scale molecular dynamic simulations combined with accurate binding free energy calculations. *Nanoscale* **2021**, *13*, 8313–8332. [CrossRef]

64. Pavlova, A.; Lynch, D.L.; Daidone, I.; Zanetti-Polzi, L.; Smith, M.D.; Chipot, C.; Kneller, D.W.; Kovalevsky, A.; Coates, L.; Golosov, A.A.; et al. Inhibitor binding influences the protonation states of histidines in SARS-CoV-2 main protease. *Chem. Sci.* **2021**, *12*, 1513–1527. [CrossRef]

65. Kneller, D.W.; Phillips, G.; Weiss, K.L.; Zhang, Q.; Coates, L.; Kovalevsky, A. Direct Observation of Protonation State Modulation in SARS-CoV-2 Main Protease upon Inhibitor Binding with Neutron Crystallography. *J. Med. Chem.* **2021**, *64*, 4991–5000. [CrossRef]

66. Chan, H.T.H.; Moesser, M.A.; Walters, R.K.; Malla, T.R.; Twidale, R.M.; John, T.; Deeks, H.M.; Johnston-Wood, T.; Mikhailov, V.; Sessions, R.B.; et al. Discovery of SARS-CoV-2 Mpropeptide inhibitors from modelling substrate and ligand binding. *Chem. Sci.* **2021**, *12*, 13686–13703. [CrossRef]

67. Kneller, D.W.; Phillips, G.; Weiss, K.L.; Pant, S.; Zhang, Q.; O'Neill, H.M.; Coates, L.; Kovalevsky, A. Unusual zwitterionic catalytic site of SARS-CoV-2 main protease revealed by neutron crystallography. *J. Biol. Chem.* **2020**, *295*, 17365–17373. [CrossRef]

68. Ramos-Guzmán, C.A.; Ruiz-Pernía, J.J.; Tuñón, I. Unraveling the SARS-CoV-2 Main Protease Mechanism Using Multiscale Methods. *ACS Catal.* **2020**, *10*, 12544–12554. [CrossRef]

69. Arafet, K.; Serrano-Aparicio, N.; Lodola, A.; Mulholland, A.J.; González, F.V.; Świderek, K.; Moliner, V. Mechanism of inhibition of SARS-CoV-2 MprobyN3peptidyl Michael acceptor explained by QM/MM simulations and design of new derivatives with tunable chemical reactivity. *Chem. Sci.* **2021**, *12*, 1433–1444. [CrossRef]

70. Maier, J.; Martinez, C.; Kasavajhala, K.; Wickstrom, L.; Hauser, K.E.; Simmerling, C. ff14SB: Improving the Accuracy of Protein Side Chain and Backbone Parameters from ff99SB. *J. Chem. Theory Comput.* **2015**, *11*, 3696–3713. [CrossRef]

71. Case, D.A.; Betz, R.M.; Botello-Smith, W.; Cerutti, D.S.; Cheatham, I.T.E.; Darden, T.A.; Duke, R.E.; Giese, T.J.; Gohlke, H.; Goetz, A.W.; et al. *Amber 16*; University of California: San Francisco, CA, USA, 2016.

72. Schneidman-Duhovny, D.; Inbar, Y.; Nussinov, R.; Wolfson, H.J. PatchDock and SymmDock: Servers for rigid and symmetric docking. *Nucleic Acids Res.* **2005**, *33*, 363–367. [CrossRef]

73. Miller, B.R.; McGee, T.D.; Swails, J.M.; Homeyer, N.; Gohlke, H.; Roitberg, A.E. MMPBSA.py: An efficient program for end-state free energy calculations. *J. Chem. Theory Comput.* **2012**, *8*, 3314–3321. [CrossRef]